Nat Hazards (2011) 58:1311–1332
DOI 10.1007/s11069-011-9734-7

ORIGINAL PAPER

Using differential SAR interferometry to map land subsidence: a case study in the Pingtung Plain of SW Taiwan

Chia-Sheng Hsieh · Tian-Yuan Shih · Jyr-Ching Hu · Hsin Tung · Mong-Han Huang · Jacques Angelier

Received: 10 July 2009 / Accepted: 27 January 2011 / Published online: 18 February 2011

Abstract Synthetic aperture radar (SAR) interferometry (InSAR) is a geodetic tool widely applied in the studies of earth-surface deformation. This technique has the benefits of high spatial resolution and centimetre-scale accuracy. Differential SAR interferometry (DInSAR) is used to measure ground deformation with repeat-pass SAR images. This study applied DInSAR and persistent scatterers InSAR (PSInSAR) for detecting land subsidence in the Pingtung Plain, southern Taiwan, between 1995 and 2000. In recent years, serious land subsidence occurred along coastal regions of Taiwan as a consequence of over-pumping of underground water. Results of this study revealed that the critical subsidence region is located on the coast near the estuary of Linpien River. It is also found that subsidence was significantly higher during the dry season than the wet season. The maximum annual subsidence rate of the dry season is up to −11.51 cm/year in critical subsidence region and the vertical land movement rate is much slower during the wet season. The average subsidence rates in wet and dry seasons are −0.31 and −3.37 cm/year, respectively. As a result, the subsidence rate in dry seasons is about 3 cm larger than in wet seasons.

Keywords SAR inteferometry · DInSAR · PSInSAR · Land subsidence · Pingtung Plain

C.-S. Hsieh
Department of Civil Engineering, National Kaohsiung University of Applied Sciences, Kaohsiung, Taiwan

T.-Y. Shih (✉)
Department of Civil Engineering, National Chiao-Tung University, Hsinchu, Taiwan
e-mail: tyshih@mail.nctu.edu.tw

J.-C. Hu · H. Tung
Department of Geosciences, National Taiwan University, Taipei, Taiwan

M.-H. Huang
Berkeley Seismological Laboratory, University of California, Berkeley, CA, USA

J. Angelier
Observatoire Océanologique de Villefranche, Géosciences Azur, Villefranche-sur-Mer, France

1 Introduction

The interferometric synthetic aperture radar (InSAR) technique allows generation of high-precision digital terrain data over a broad area, resulting in the production of digital elevation model (DEM). The differential SAR interferometry (DInSAR) technique can be used to determine earth-surface displacement and detect deformation arising from land subsidence, earthquakes, volcanoes, or others (Massonnet and Feigl 1998; Bürgmann et al. 2000; Zebker 2000). In addition to mandatory corrections of various effects related to orbital and climatic characteristics, the resulting DInSAR interferograms may be affected by poor image coherence caused by abrupt terrain and dense vegetation, a dire concern in Taiwan. However, several successful studies have already validated this method and mapped the Earth's surface deformation in Taiwan, including the studies regarding the uplift of the Tainan tableland (Fruneau et al. 2001; Huang et al. 2006) and the co-seismic deformation of the footwall block of the Chelungpu Fault during the 1999 Chi–Chi earthquake (Pathier et al. 2003; Chang et al. 2004b; Hsieh and Shih 2006).

Geodetic measurements using the global positioning system (GPS) and differential levelling offer high-precision control points for measuring earth-surface deformation. However, they are in the form of either points or lines. And there is practical limitation on the density of geodetic points. To this respect, for analysing the active deformation of a given area, it is appropriate to integrate geodetic measurements with DInSAR, which provides areal measurements.

The Pingtung Plain of south-western Taiwan is a fast subsidence domain with high sedimentation rate (Hsieh et al. 2006). These characteristics arise from the particular tectonic setting of the area (Hu et al. 2006, 2007). Although human activities such as over-pumping of ground water significantly increase the present subsidence rate (Hou et al. 2005), the main origin of Quaternary subsidence is the extension related to lateral escape near the southern tip of the Taiwan collision belt (Angelier et al. 2009). Both horizontal and vertical land movement rates are high in this area. In this study, DInSAR and PSInSAR are applied together with GPS and levelling for further exploring land subsidence. The result of this study reveals that it is uplifting in the northern Pingtung Plain and subsiding in the southern Pingtung Plain. It is also found that the subsidence rate is significantly higher in dry seasons than in wet seasons.

2 Tectonic background

As shown in Fig. 1, Taiwan is located at the boundary between the south-east portion of the Eurasian Plate and the Philippine Sea Plate, where the convergent rate between the volcanic arc and continental margin is about 8.2 cm/year (Yu et al. 1997; Lin et al. 2010). Because of arc–continent collision (Suppe 1984), the island of Taiwan is the result of active orogenic mountain building with major crustal shortening (Ho 1986). The Pingtung Plain is located in south-western Taiwan (Fig. 1) and covers a nearly rectangular area of 1,210 km^2. It corresponds to a major graben bounded by two large faults (Fig. 2): the Chaochou fault to the east (as the western boundary of the metamorphic formations of the Central Range) and the Kaoping fault to the west (in the Late Cenozoic formations of the Foothills). Whereas the Chaouchou fault is well exposed at the foot of high mountains, the Kaoping fault is often buried beneath the Holocene alluvium of the Kaoping River. All outcrops in the Pingtung Plain, as well as shallow wells (Hsieh et al. 2006), show unconsolidated sediments of the late Pleistocene and the Holocene (Fig. 2). Most of these

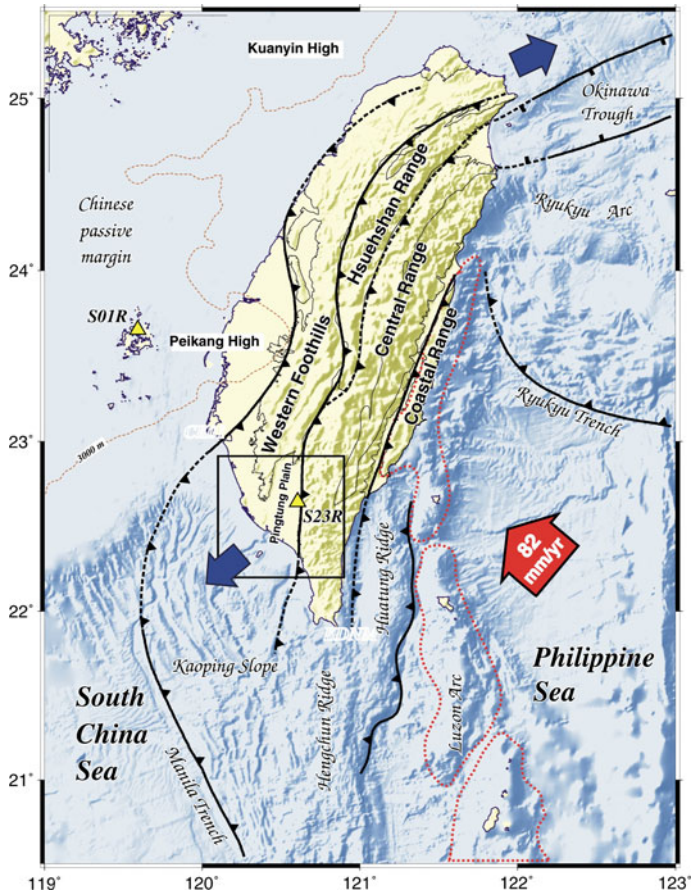

Fig. 1 Geotectonic framework and major structural units of Taiwan between the Eurasian and Philippine Sea plate. The large *red arrow* shows the direction and velocity of convergence between the volcanic arc and the continental margin (Yu et al. 1997). *Blue arrows* indicate the directions of tectonic escape. The *green area* denotes the location of basement high, and its surrounding *brown dash line* indicates the 3-km-deep top of the pre-Tertiary basement (Lin et al. 2003). Red domains are the Luzon volcanic arcs. *Yellow triangles* present the locations of local permanent GPS stations used in this study. The *rectangle* denotes the study area

sediments consist of coastal and estuarine sand and mud, with abundant shallow-marine and lagoon shells and foraminifera (Shyu et al. 2005). East of the Chaochou fault, the high mountains are mainly composed of Eocene–Miocene argillite, slate and meta-sandstone. The most significant geomorphological feature of the Pingtung Plain, easily observed from the satellite images of Taiwan, is the straight, N–S trending Chaochou fault escarpment that separates the alluvial plain from the high mountains (Fig. 2). Geological, seismological and geodetic observations suggest that this Chaochou Fault is a reverse fault with a left-lateral component (Hu et al. 1997, 2001, 2007). To the north and west, the Pingtung Plain is bounded by low hills of deformed Quaternary sediments. The Kaoping River flows along this western edge, which corresponds to the trace of the Kaoping Fault. Geodetic observations (Hu et al. 2006) indicate a right-lateral component of present-day slip along

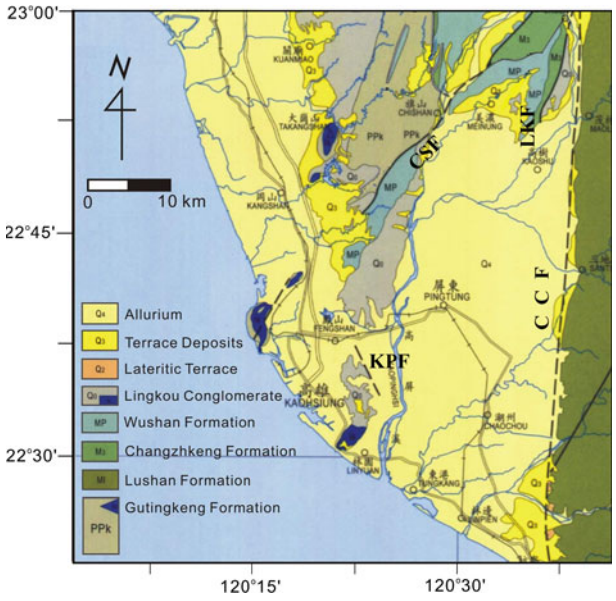

Fig. 2 Neotectonic map of south-western Taiwan of the study area (modified after Hu et al. 2006). *Thick lines* indicate the active faults. *CCF* Chaochou Fault, *CSF* Chishan Fault, *LKF* Liukuei Fault, *KPF* Kaoping Fault. The *dashed line* indicates the inferred fault

the Kaoping Fault, in excellent agreement with the interpretation in terms of extrusion and lateral escape affecting the Pingtung Plain area.

The Pingtung GPS network (Hou et al. 2005) was established in 1995. There are 49 stations, with one continuous observing station (S23R) and 48 campaign-mode stations. It was thus shown that the present-day rate of horizontal displacement relative to the Paisha station (S01R) of the Penghu archipelago (Yu et al. 1997) falls in the range of 42.2–55.5 mm/year depending on the configuration of stations selected (Hu et al. 2006; Shen et al. 2003), towards azimuth from 247.1° to 272.5° (Hu et al. 2007). The choice of the S01R station as a reference is quite appropriate, because this station belongs to the stable area of the Taiwan Strait, that is, the continental foreland of the Taiwan belt. These relatively high rates of displacement are not surprising, because the Pingtung Plain area is bounded to the west by an actively deforming front zone of the western foothills, on the eastern side of the foreland basin system (Chiang et al. 2004). Both the geological information about Quaternary tectonics and the geodetic data about present-day movements indicate that the Pingtung Plain is subject to active horizontal and vertical land movement.

Serious vertical land movement, reaching −25 mm/year, has recently been observed along the coastal region near the estuary of the Linpien River (south-eastern Pingtung Plain), mainly as a consequence of over-pumping of underground water. As Fig. 3 shows, for the whole Pingtung Plain, the vertical land movement rates measured at the surface between 1996 and 1999 fall in the range +13 to −25 mm/year (positive for uplift, negative for subsidence). The highest subsidence rates affected 20 stations of the southern Pingtung Plain (Hu et al. 2006). For the 11 stations of the southern Pingtung Plain closest to the sea, east of the Kaoping River and west of the Chaouchou Fault, the vertical land movement rates of the period 1995–2005 range from −7 to −28 mm/year, with an average value of

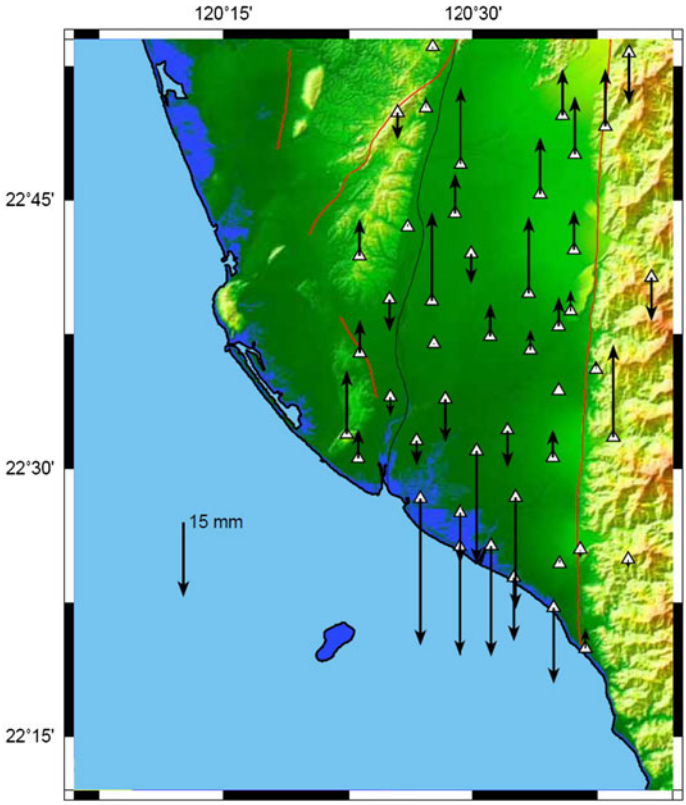

Fig. 3 Vertical velocities of GPS stations in the Pingtung Plain relative to Paisha, Penghu (S01R), from 1996 to 1999. *Thick lines* are active faults. Shaded topography is based on 40 m × 40 m DEM

−17 mm/year. In more detail, some seasonal changes in surface subsidence rate in the Pingtung Plain have been observed by Chang et al. (2004a) using the InSAR technique, which was interpreted as caused by the fluctuations of water table level. How far these present-day rates, which are affected by human activity, can be extrapolated in the past is a crucial issue. According to a geological study of drill cores conducted by the Taiwan Geological Survey in the Pingtung Plain, the southern area has a long-term subsidence rate of about +6 mm/year on average (Lai et al. 2002). The comparison between this long-term Holocene rate and the average present-day rate in the same area suggests that the tectonic origin may account for roughly one-third of the total subsidence in the coastal area.

3 Differential interferometry (DInSAR) analysis

3.1 The method

InSAR is a technique for extracting information about changes in the surface of the Earth using the phase contents of the radar signal. The use of the interferometric technique for the retrieval of terrain deformations requires the SAR images to be taken from exactly the same position in space at two different times. Reliable interference between SAR images in

the same area is possible only after meeting all relevant conditions. A major limitation is that image pairs yield interference only when the base length is less than the critical value. The sensitivity of InSAR depends upon the observed geometric relationship, while the base length affects the magnitude of noise. When the baseline is too short, the sensitivity to detect changes in terrain may be lost. Otherwise, the de-correlation of the baseline yields phase errors (Zebker and Villasenor 1992).

DInSAR uses two InSAR interference patterns from different times, one named as topographic pair indicating the elevation of the Earth's surface and the other named as deformation pair containing both terrain effects and surface deformation. The two interference patterns are then differentiated to remove the terrain effect, and the ultimate result represents the phase difference caused by deformation of the earth surface. This technology provides relatively good accuracy at the centimetre scale (Gabriel et al. 1989).

Because different types of topographic pairs exist, DInSAR offers three processing methods: two-pass, three-pass and four-pass (Massonnet et al. 1994; Zebker et al. 1994; Massonnet and Feigl, 1998; Colesanti et al. 2003; Chang et al. 2004a, b, 2010; Ding et al., 2004; Huang et al. 2006, 2009). The processing of SAR interferometric data is a complex procedure. Based on the quality of the data sets, the performance of each processing step is crucial. To summarise, the interferometric processing consists of the following steps: (1) image registration, (2) calculation of modulate phase difference, (3) phase unwrapping and geocoding (Gens and Genderen 1996; Klees and Massonnet 1998; Rosen et al. 2000).

It is worth noting that the displacement measured by DInSAR is in the line-of-sight direction, not vertical direction. In our case, the line of sight of the satellite is trending nearly E–W, with a westward deviation of about 19°–26°. This means that the interferometric pattern is mainly influenced by the vertical component of ground displacement. As a consequence, our analysis is suitable for detecting vertical motion and would not be appropriate for detecting the strike-slip components that exist along the faults of the Pingtung Basin (which trend N–S, nearly parallel to orbits). Every colour change in the fringe interference pattern indicates a distance change of 28 mm along the line of sight, that is, one half of the ERS-1 satellite wavelength (Massonnet et al. 1994).

In this study, we proceeded the interferograms by using the CNES DIAPASON (differential interferometric automated process applied to survey of nature) software with a two-pass approach. Interferograms phase unwrapping was done by using the SNAPHU software (Chen and Zebker 2000). The topography was estimated and extracted from SRTM (shuttle radar topography mission) DEM (Stevens and Wadge 2004; Peyret et al. 2008).

3.2 Data acquisition

The ERS 1/2 radar system, operating at a wavelength of 5.6 cm, provides images of Earth's surface from an altitude of about 790 km and produces radar backscatter maps of 100-km-wide swaths at a resolution of about 25 m across track and 6 m along track. We collected ERS 1/2 radar signal samples acquired over the Pingtung area during the period 1995–2000. To efficiently explore surface deformation in the Pingtung Plain, we selected suitable image pairs with the DESCW (Display Earth remote sensing Swath Coverage for Windows) program from European Space Agency (ERS). In total, thirteen ERS 1/2 satellite images are used. Ten image pairs were identified as suitable for interference. The corresponding base length and time interval are listed in Table 1. The baseline met the requirements for interference, with a time interval from 36 to 385 days and a time slot of 1995–2000.

Table 1 Image pair schedule

Image pair			Orbit	Horizontal baseline (m)	Vertical baseline (m)	Time interval (day)
No.	Mission	Image pair				
1	E1	19950705	20761	−66	−56	141
	E2	19951123	3092			
2	E1	19960131	23767	60	5	106
	E2	19960516	5597			
3	E1	19960410	24769	1	−103	36
	E2	19960516	5597			
4	E2	19970501	10607	14	59	315
	E2	19980312	15116			
5	E2	19980312	15116	−37	−99	385
	E2	19990401	20627			
6	E2	19981112	18623	−38	−19	70
	E2	19990121	19625			
7	E2	19981112	18623	48	84	175
	E2	19990506	21128			
8	E2	19990121	19625	84	98	105
	E2	19990506	21128			
9	E2	19990506	21128	−34	−34	175
	E2	19991028	23633			
10	E2	19990506	21128	−814	−1,024	245
	E2	20000106	24635			

3.3 Results

Pingtung Plain is located in southern Taiwan, a subtropical zone where rainfall varies substantially between seasons. The rainfall between 1995 and 2000 showed distinct wet and dry seasons in the Pingtung area (Fig. 4). The wet season is characterised by monthly rainfall exceeding 200 mm from May to October, whereas the dry season experiences very little rainfall from November to April. This aspect deserves consideration because rainfall might affect surface subsidence. We consequently divided the interference patterns into wet and dry seasons (Table 3), based on time-dependent deformation. The interferograms are shown with the mask for extremely low coherence values, and we separately present the interferograms for the dry season (Fig. 5) and the wet season (Fig. 6). Note, however, that the time periods differ; whereas for the dry season they remain in a range of 2.3–5.8 months (3.8 months on average), for the wet season two contrasting ranges exist, 4.6–5.7 months and 8.0–10.4 months. This means that the longest two periods include part of the dry season (on the contrary, there is no part of the wet season contained in a couple of the dry season category). Note also that in each of the dry season and wet season categories, the first image is the same in two image pairs. These contrasts in time difference should be kept in mind while comparing the results.

Significant differences exist between the dry season and wet season interferograms. Figure 5 (dry season category) clearly reveals subsidence in the coastal area of southeastern Pingtung Plain (near the estuary of the Linpien River), whereas this aspect is

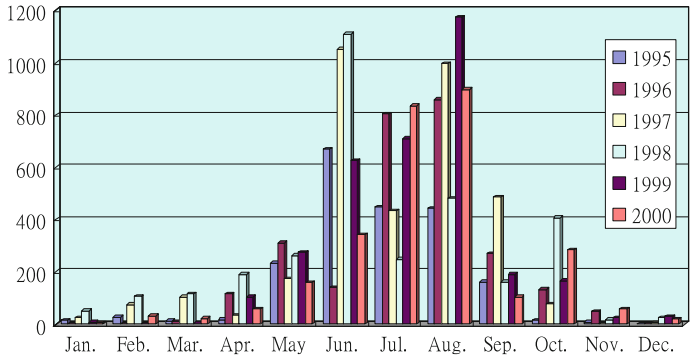

Fig. 4 Rainfall between 1995 and 2000 in the Pingtung area of Taiwan. The wet season occurs in May–October, while the dry season occurs in November–April. Data were obtained from the Central Weather Bureau of Taiwan

present but poorly illustrated for other interferograms (Fig. 6). This difference is consistent with the lower level of water tables during the dry season, which enhances subsidence. Our interferograms provide little information concerning the behaviour of the Chaochou fault, which is out of the mapped region. In contrast, regardless of the season, all interferograms reveal the presence of an N–S boundary along the western edge of the Pingtung basin, coincident with the expected position of the Kaoping fault (Figs. 5 and 6). Not surprisingly, the fringe pattern across this boundary is consistent with larger subsidence on the eastern side (the Pingtung basin). The surprising finding is the presence of another N–S boundary inside the Pingtung basin, especially visible on some interferograms of the dry season (Fig. 5). In a more general way, the interferograms of Fig. 5 (dry season) show more impressive differential interference patterns, when compared with those of Fig. 6 (wet season). This contrast is partly attributable to the shorter time intervals and the smaller variations in water contents near the surface. The interference pattern of the wet season has a poorer interference effect because of a longer time interval spanning the entire wet season. Despite these limitations, some fringes indicate that a major subsidence centre of the Pingtung Basin is located near the lower Linpien River, with a decreasing subsidence towards east and west as well as to the north, which is consistent with the information provided by the dry season interferograms.

3.4 Comparison of GPS data and levelling results

As mentioned earlier, the radar technique is sensitive to the line-of-sight component of motion. Thus, the results obtained from DInSAR are slant range displacement (SRD) values, rather than actual height changes. With accurate GPS horizontal displacement data and the geometric relationship, it is possible to obtain vertical height changes.

As illustrated in Fig. 7, the GPS horizontal displacement vector $\mathbf{V} = (a, b, 0)$, and the angle between the satellite orbit and north (N) $= \theta$. It is necessary to project GPS vertical displacement vectors (a', b', c') into satellite directions according to the formula:

$$\begin{bmatrix} a' \\ b' \\ c' \end{bmatrix} = \begin{bmatrix} \cos\phi & \sin\phi & 0 \\ -\sin\phi & \cos\phi & 0 \\ 0 & 0 & 1 \end{bmatrix} \begin{bmatrix} a \\ b \\ c \end{bmatrix} = \begin{bmatrix} a\cos\phi + b\sin\phi \\ -a\sin\phi + b\cos\phi \\ c \end{bmatrix}. \quad (1)$$

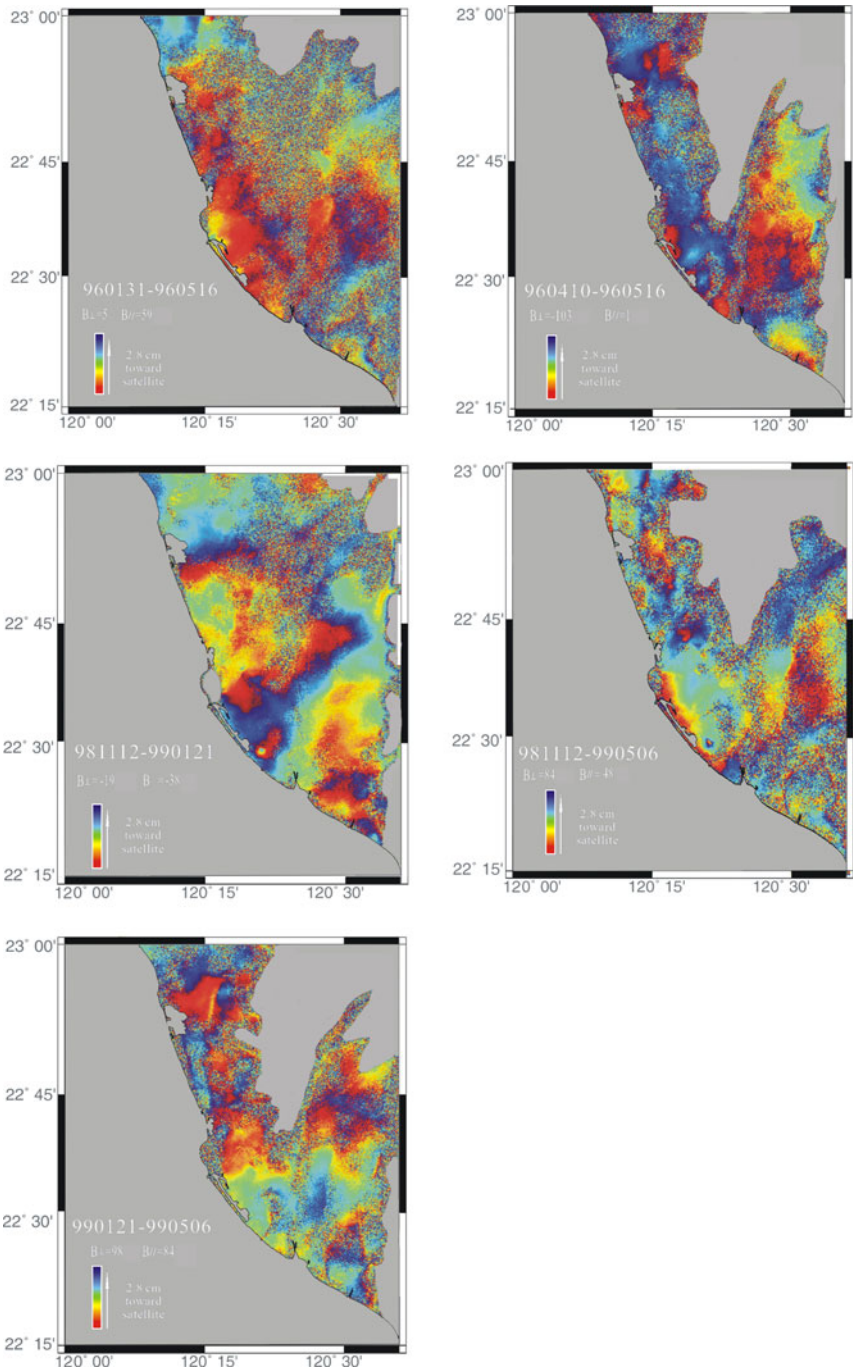

Fig. 5 Differential interference results for image pairs in the dry season. The fringe of the differential interference pattern represents the deformation along the satellite direction. A colour shift from *red to blue* indicates a change of +2.8 cm. A colour shift from *blue to red* indicates a change of −2.8 cm. The legends in the *lower left* represent date, *vertical/horizontal* base length and fringe scale

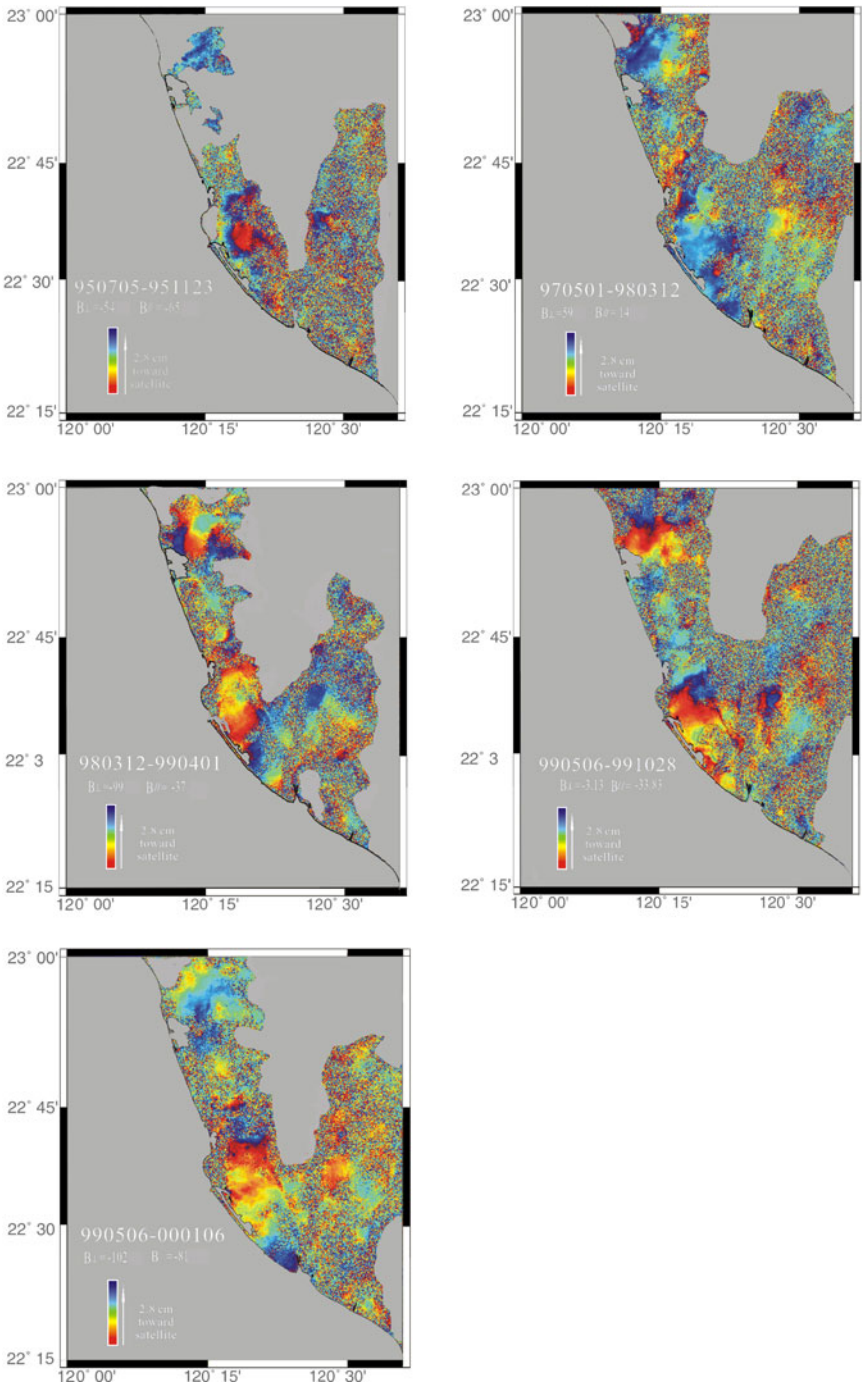

Fig. 6 Differential interference results for image pairs in the wet season or during a longer time interval. Despite the obscure fringe, it is clear that the residence centre of the Pingtung Plain is at the mouth of the Linpien and declines towards the two sides and to the north

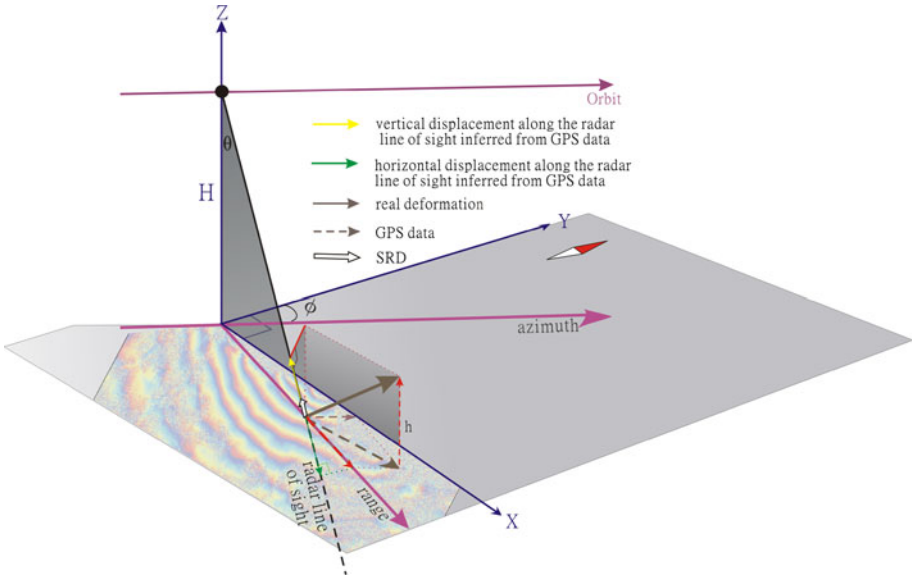

Fig. 7 Schematic drawing of the geometric relationships among GPS, SRD and real deformation. The SRD (slant range displacement) is subtracted for the projection of real deformation along the *radar line*-of-sight direction

Next, GPS horizontal displacement vectors are projected in the satellite direction, and SRD (Slant Range Displacement) is subtracted for the projection of real deformation along the radar line-of-sight direction:

$$\Delta r = (a\cos\phi + b\sin\phi)\sin\theta + c\cos\theta, \tag{2}$$

$$h = \Delta r \sec\theta - (a\cos\phi + b\sin\phi)\tan\theta, \tag{3}$$

where Δr = SRD, the differential interference pattern. The vertical displacement, h, is obtained from Eq. 3.

To validate the vertical elevation changes revealed by differential interferometry and evaluate their accuracy, we selected the levelling data measured by the Energy and Resources Laboratories (ERL) of the Industrial Technology Research Institute (ITRI) in April 1997 and March 1998 (ITRI 1998). The fixed station (BM25) is located in the Henchun Peninsular and is considered as a geologically stable region without land subsidence. Two levelling lines were used. Line A was located in the north and includes 10 benchmark stations (A1–A10 in Fig. 8); line B was located in the south, close to the coast, with 6 stations (B1–B6 in Fig. 8). The levelling time span was April 1997–March 1998; therefore, the GPS height data in the same period were used as a baseline. The comparison of height changes along the levelling lines A and B is shown in Fig. 9a, b, respectively.

In line A, the result obtained from DInSAR is substantially different from the levelling when near the west tip of the chart, with a maximum misfit of 4.69 cm/year at station A1 and minimum misfit of 0.33 cm/year at station A5. The root mean square (rms) value of the differences of DInSAR and levelling along these profiles is 2.40 cm/year. The result obtained from DInSAR is different from the GPS with a maximum misfit of 1.97 cm/year at station A1 and minimum misfit of 0.30 cm/year at station A10. The rms value of the differences of DInSAR and GPS is 1.25 cm/year (Fig. 9a). The average vertical

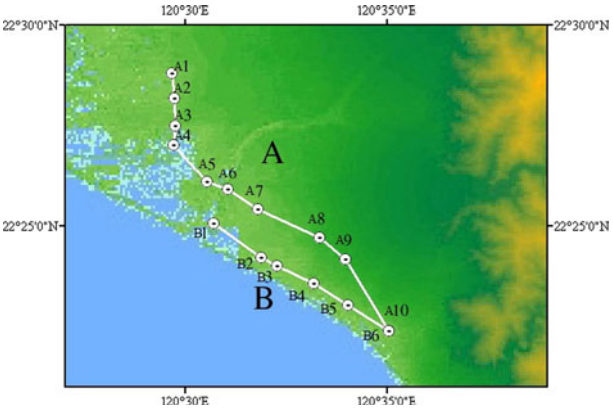

Fig. 8 Distribution map of levelling points. *Line A* comprises 10 stations; *line B* comprises 6 stations

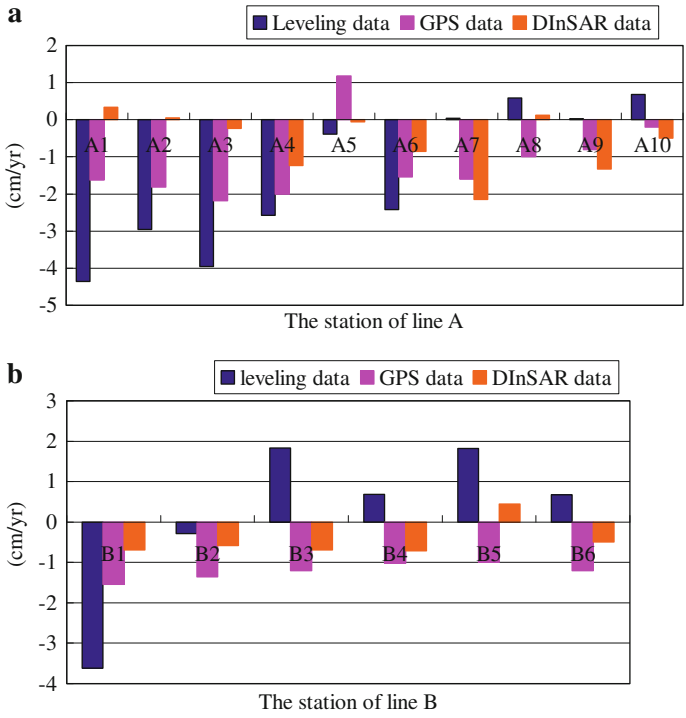

Fig. 9 **a** The bar chart of height changes based on levelling data, GPS and DInSAR results of measuring *line A*. **b** The bar chart of height changes based on levelling data, GPS and DInSAR results of measuring *line B*

deformation change rate for the ten levelling stations is −1.53 cm/year for levelling, −1.16 cm/year for GPS and −0.58 cm/year for DInSAR. The average differences in annual deformation rate between DInSAR and levelling and between DInSAR and GPS

were 0.95 cm/year and 0.57 cm/year, respectively. All results concur to indicate that the point A5, located near the Linpien River, shows a specific behaviour without subsidence.

In line B, the result obtained from DInSAR is substantially different from the levelling with a maximum misfit of 2.93 cm/year at station B1 and minimum misfit of 0.30 cm/year at station B2. The rms value of the differences of DInSAR and levelling is 1.83 cm/year. The result obtained from DInSAR is different from the GPS with a maximum misfit of 1.45 cm/year at station A1 and minimum misfit of 0.30 cm/year at station B2. The rms value of the differences of DInSAR and GPS is 0.84 cm/year (Fig. 9b). The average vertical deformation change rate for the six levelling stations is +0.18 cm/year for levelling, −1.22 cm/year for GPS and −0.46 cm/year for DInSAR. The average differences in annual deformation rate between DInSAR and levelling and between DInSAR and GPS were 0.64 cm/year and 0.76 cm/year, respectively.

The differences in elevation changes detected in profiles A and B cannot be considered negligible, but it is worth noting that only the levelling was done at the benchmarks, while the elevation changes obtained for GPS and DInSAR result from extrapolation of data at nearby localities (GPS) or mapping (DInSAR). This certainly results in additional discrepancies.

4 Persistent scatterer analysis

4.1 The method and data acquisition

The DInSAR technique can provide excellent observations in flat area with high temporal correlation (e.g. man-made buildings, bed rocks). However, in the regions with dense vegetation (e.g. rice field) or high relief (e.g. mountains), the conventional DInSAR is unable to obtain reliable signals in these regions due to the lower correlation between acquisitions. The persistent scatterers (PS) InSAR is an advanced technique in comparison with conventional InSAR technique, which is able to overcome the problems of decorrelation when generating a time series of phase changes without atmospheric and DEM residual effects by computing only on sparsely distributed PSs who are pixels coherent over long time series. This technique has been developed in the late 1990s by A. Ferretti, F. Rocca and C. Prati of the Technical University of Milan (POLIMI). The first algorithm to find out the PS pixels was brought up by Ferretti et al. (2000, 2001), and trademarked it as the ''Permanent Scatterer technique^{TM}''. After that, similar processing algorithms have since been developed by Crosetto et al. (2003) and Kampes (2005). Besides, the SBAS (small baseline subset) technique developed by Berardino et al. (2002) and StaMPS (Stanford method for persistent scatterers) developed by Hooper et al. (2004) are also based on the same idea of PSInSAR technique with different name. In addition, several studies have been successfully applied by using this technique to demonstrate deformation in Taiwan (Chang et al. 2010; Tung and Hu 2011).

In this study, we use 31 ERS-1 and ERS-2 C-band (radar wavelength is ~5.6 cm) data from European Space Agency (ESA) from January 1996 to August 1999. These descending scenes in track 232 are used to generating 30 interferograms (Table 2). The interferometric processing is carried out with the Diapason software developed by Centre National d'Etudes Spatiales (CNES). The SRTM DEM from NASA is used to remove the phase due to topography. In particular, the Delft Institute for Earth-Oriented Space Research (DEOS) precise orbital data were injected in interferometric processing to further remove the orbital uncertainties.

Table 2 Images used for PSInSAR analysis

No	Orbit	Date	Sensor	$B_{\perp}$(m)
1	23767	1996/01/31	ERS-1	0
2	4094	1996/02/01	ERS-2	108
3	24268	1996/03/06	ERS-1	228
4	4595	1996/03/07	ERS-2	160
5	5097	1996/04/11	ERS-2	7
6	6099	1996/06/20	ERS-2	−545
7	7100	1996/08/29	ERS-2	−866
8	7602	1996/10/03	ERS-2	−566
9	8604	1996/12/12	ERS-2	−578
10	9104	1997/01/16	ERS-2	−227
11	9606	1997/02/20	ERS-2	−411
12	10106	1997/03/27	ERS-2	−157
13	10607	1997/05/01	ERS-2	−613
14	11609	1997/07/10	ERS-2	−442
15	12111	1997/08/14	ERS-2	−186
16	12611	1997/09/18	ERS-2	−700
17	13613	1997/11/27	ERS-2	−70
18	14114	1998/01/01	ERS-2	8
19	14616	1998/02/05	ERS-2	−519
20	15117	1998/03/12	ERS-2	−554
21	16118	1998/05/21	ERS-2	−255
22	17121	1998/07/30	ERS-2	−124
23	17622	1998/09/03	ERS-2	20
24	18623	1998/11/12	ERS-2	64
25	19125	1998/12/17	ERS-2	−724
26	19625	1999/01/21	ERS-2	64
27	20627	1999/04/01	ERS-2	−653
28	21128	1999/05/06	ERS-2	156
29	21630	1999/06/10	ERS-2	−254
30	22130	1999/07/15	ERS-2	−101
31	22631	1999/08/19	ERS-2	932

The master image is fixed on 1997/07/10. Perpendicular baseline is relative to 19960131 (orbit: 23767)

4.2 Results

To illustrate the vertical land movement in the Pingtung Plain, Fig. 10 shows the contour of deformation from the interpolation of GPS data (Hu et al. 2006) and the average deformation map calculated from our PSInSAR analysis (data from 1996 to 1999). The colour scale represents the annual displacement rate along the line of sight. Comparing Fig. 10a and b, there is a good consistency regarding the shape of the land subsidence area in the southern Pingtung Plain and also that of the uplift area of the northern Pingtung Plain.

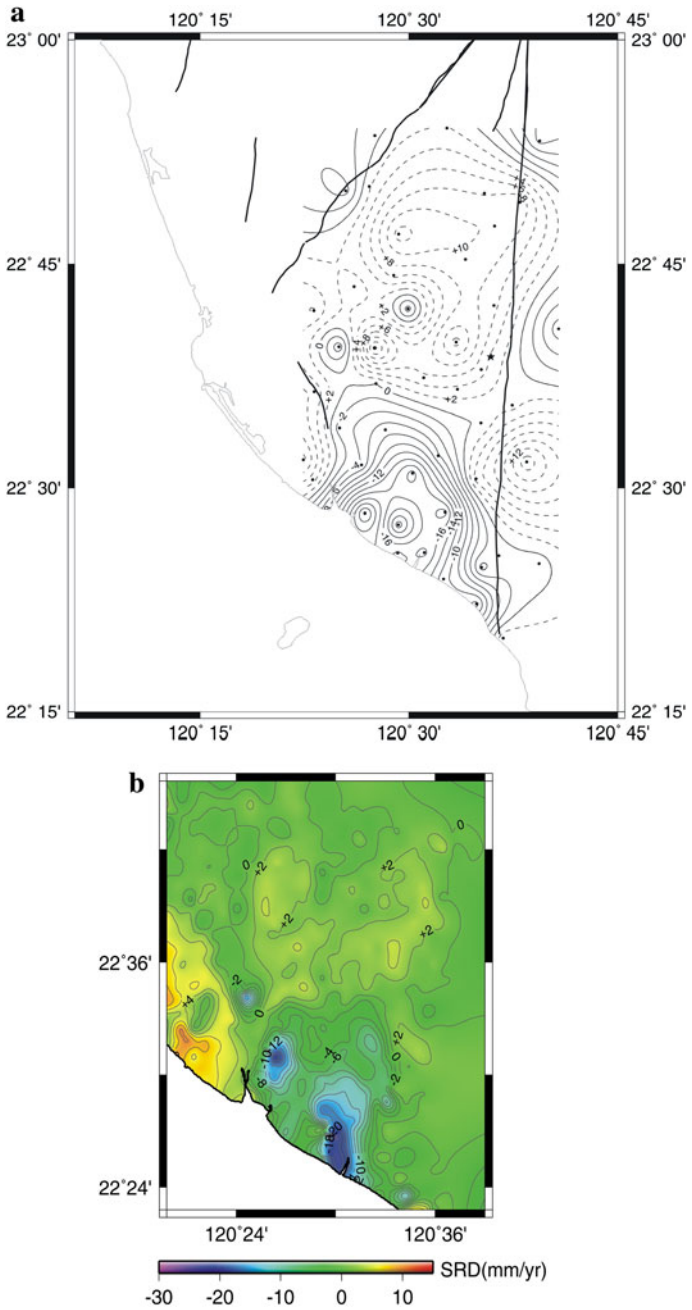

Fig. 10 **a** Annual uplift and subsidence rate from interpolation of GPS data. Contours of vertical velocities of GPS stations in the Pingtung Plain relative to Paisha, Penghu (S01R), from 1996 to 1999. Contour interval is 2 mm/year. *Dotted contours* indicate uplift and *solid contours* are subsidence. *Solid star* indicates permanent GPS station. *Solid circles* are survey mode stations. *Thick lines* are active faults (data from Hu et al. 2006). **b** The average deformation map by PSs of the study area from 1996 to 1999. The negative SRD rate represents land subsidence and positive ones represent uplift. Contour interval is 2 mm/year

Uplift prevails in the northern Pingtung Plain, with velocities up to +6 mm/year. In contrast, the fringes show rapid subsidence in the southern Pingtung Plain near the coast, with rates −20 mm/year. Moreover, both maps highlight the land movement along the Kaoping fault zone that bounds the Pingtung Plain to the west. On the contrary, there is no clear expression of the N–S lineament inside the Pingtung Plain, which was identified in some of our interferograms (Fig. 6).

5 Analysis of subsidence in the Pingtung Plain

To characterise better the vertical land movement in the southern Pingtung area, which was mainly interested in, four cross-sections were drawn. The location of profiles is shown in Fig. 11. The vertical land movement along these cross-sections is illustrated in Fig. 12a for the dry season and b for the wet season, respectively. In a more general way, the profiles extracted from interferograms in dry seasons show more substantial subsidence (Fig. 12a), in comparison with those in wet seasons (Fig. 12b). The difference is mainly due to the poorer spatial correlation of the interferograms in wet seasons.

Because the pair 980312–990401 spans both dry and wet seasons, in contrast to pair 960410–960516 that spans just 35 days, to describe the subsidence changes with time, only four pairs of images corresponding to successive time spans are selected, and the related values is presented with different symbols in the profiles.

Not surprisingly, the profiles that trend nearly perpendicular to the axis of the Pingtung Plain clearly illustrate the maximum subsidence zone, whereas the other two profiles rather illustrate the decreasing average subsidence from south to north. The profiles were picked up for the comparison of different land subsidence rates in different area. The profile C–C′ (Fig. 12a) highlights a relatively consistent subsidence tendency from 1996 to 1999, in the centre and eastern part of the Pingtung Plain. The maximum annual subsidence rate between 1998 and 1999 was about 6 cm/year. The data of the 1998–1999 periods suggest

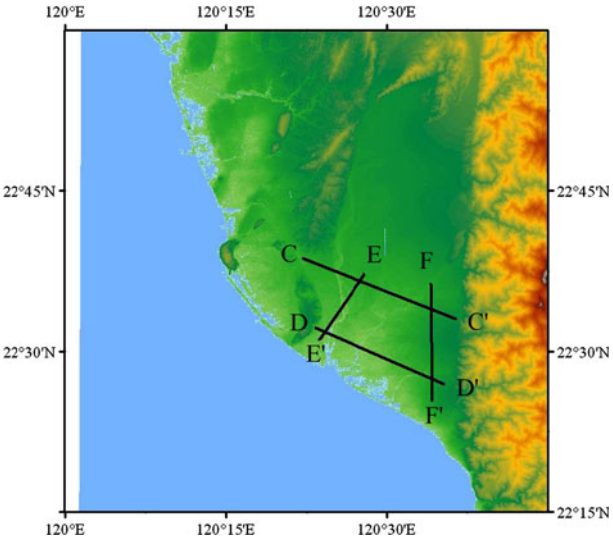

Fig. 11 The drawing map of cross-sectional C–C′, D–D′, E–E′ and F–F′

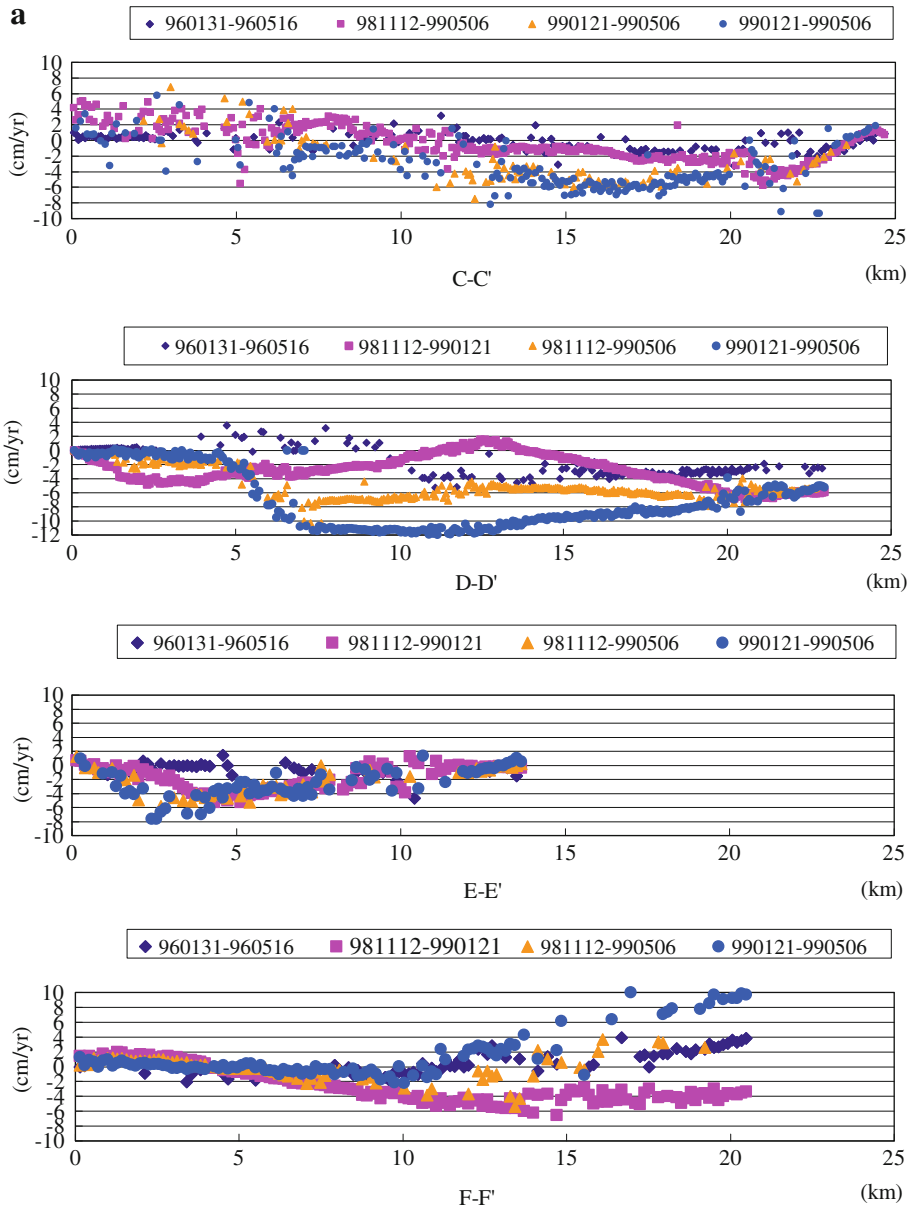

Fig. 12 **a** The deformation of cross-sections C–C′, D–D′, E–E′ and F–F′ during the dry season. The *horizontal axis* indicates the length of the cross-section (km); the *longitudinal axis* indicates the annual land deformation rates (cm/year). **b** The deformation of cross-sections C–C′, D–D′, E–E′ and F–F′ during the wet season. The *horizontal axis* indicates the length of the cross-section (km); the longitudinal axis indicates the annual land deformation rates (cm/year)

the presence of a discontinuity that coincides with the expected position of the Kaoping Fault. Comparing the profile C–C′ in Fig. 12a, b, the subsidence in the wet season shows large scattering without distinctive trends.

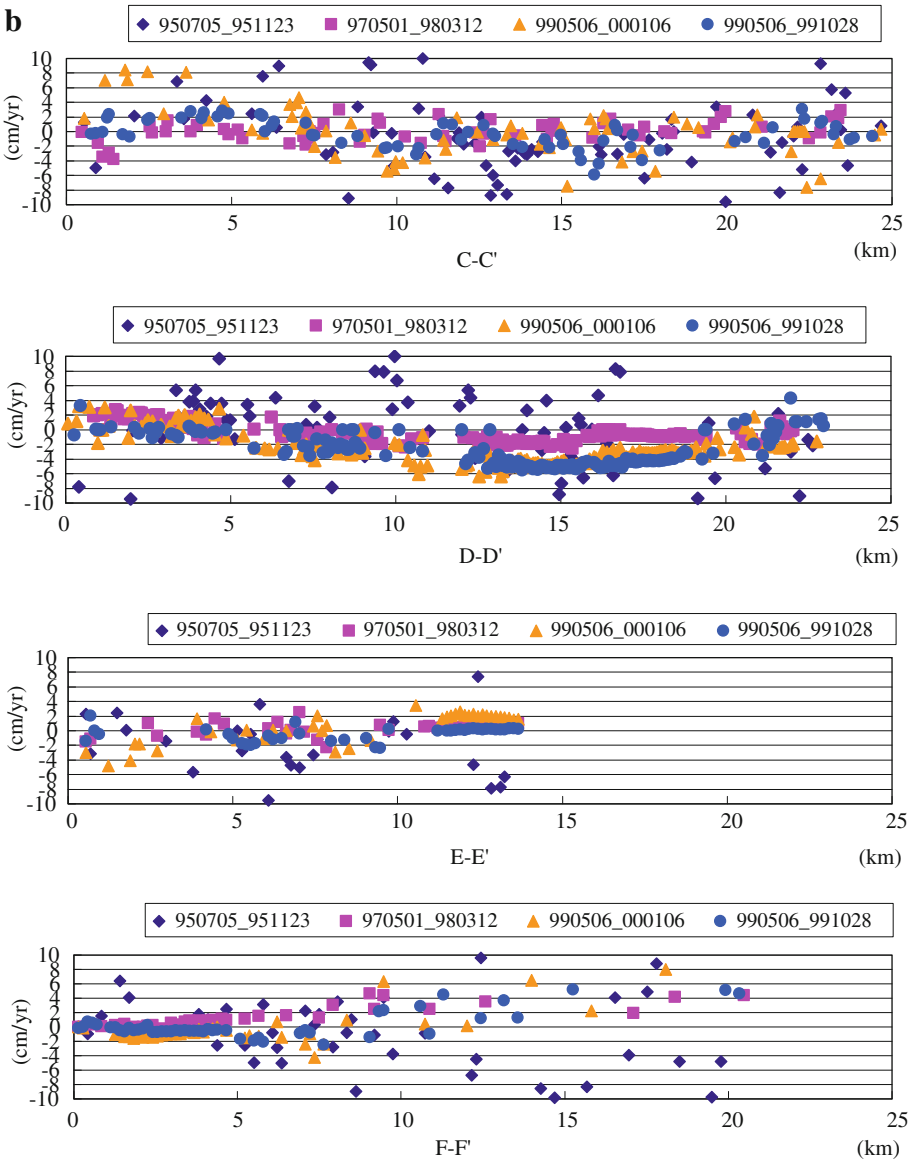

Fig. 12 continued

The cross-section D–D′ shows subsidence of about −4 cm/year between 1996 and 1998, increased up to about −12 cm/year after 1998–1999 (Fig. 12a). The figure for the wet season shows little difference relative to the dry season, but clearly reveals a similar increase in subsidence on a yearly basis (Fig. 12b). The striking difference between profiles C–C′ and D–D′ in Fig. 12b suggests that along the costal region, the surface deformation is not heavily affected by rainfall, which is not the case at a larger distance from the coast. This contrast probably results from the presence of abundant underground water near

Table 3 The maximum regional subsidence rate of image pairs in the dry and wet seasons

Wet season	Maximum regional subsidence rate (cm/year)				Dry season	Maximum regional subsidence rate (cm/year)			
Image pair	C–C′	D–D′	E–E′	F–F′	Image pair	C–C′	D–D′	E–E′	F–F′
950705–951123	−0.42	+5.05	−1.03	−0.48	960131–960516	−1.12	−1.96	−0.17	−0.64
970501–980312	+0.40	−1.31	−0.04	+3.13	981112–990121	−2.00	−1.37	−2.25	−4.33
990506–991028	−0.96	−3.51	−2.01	+0.48	981112–990506	−5.08	−6.78	−3.25	−3.24
990506–000106	−2.34	−2.34	−0.42	+0.86	990121–990506	−5.47	−11.51	−3.91	−0.69
Four pairs average	−0.83	−0.53	−0.88	+1.00	Four pairs average	−3.42	−5.41	−2.40	−2.23
Four profiles average	−0.31				Four profiles average	−3.37			

the coast. Sections E–E′ and F–F′ show that subsidence gradually varies from south to north, with increasing scattering, which is consistent with the latter observation (Table 3) about the difference between dry and wet seasons.

The four cross-sections highlight the consistency between the results from DInSAR and GPS approaches (Fig. 9). It is found from Table 3 that the maximum regional subsidence rates in the four profiles in wet seasons are −0.83, −0.53, −0.88 and +1.00 cm/year, respectively. On the other hand, the subsidence rates in dry seasons are −3.42, −5.41, −2.40 and −2.23 cm/year, respectively. The average subsidence rates for wet and dry seasons are −0.31 and −3.37 cm/year, respectively. As a result, the subsidence rate in dry seasons is about −3 cm/year larger than in wet seasons.

For cross-sections C–C′, D–D′ and E–E′, the subsidence during the wet season was much less than during the dry season, indicating that abundant rainfall replenishes underground water reservoirs. This seasonal variation of subsidence was also observed in a previous study (Chang et al. 2004a). Hu et al. (2006) pointed out that the long-term and short-term subsidence pattern is consistent with the thickness distribution of fine-grained sediments in the southern Pingtung Plain, which further explains the change in water table level (Kuo et al. 2001) between wet and dry seasons that influences the subsidence rate. In addition, the long-term subsidence and short-term subsidence show a similar pattern but with different magnitude, which illustrates the contributions of regional tectonics and hydrological effects to subsidence in the coastal area of the Pingtung Plain.

6 Discussion and conclusion

We used differential interferometry and PSInSAR to analyse SAR images of the Pingtung basin in southern Taiwan between 1995 and 2000 in order to reconstruct the spatial distribution of subsidence and its evolution with time, with additional constraints from geodetic GPS and levelling data. A comparison between these three types of data along two levelling lines revealed that despite some discrepancies, the DInSAR technology can reliably be used to deduce and map the elevation changes, with a mean difference usually less than 1 cm/year and consistent change tendencies.

Because of its potential to cover large areas rather than scattered survey points or lines, the DInSAR approach offers a better determination of the spatial extension of displacements than the levelling and GPS data. Levelling and GPS analyses accurately record

variations in topographic surface, but because of the discontinuous spatial character of observations, it commonly occurs that stations do not coincide with the most critical points of maximum uplift or subsidence or fail to account for discontinuities when compared with more gradual changes. The changes with time that we were able to identify in the southern Pingtung Plain include the contrast between dry and wet seasons for the shortest term, as well as an abrupt increase in subsidence between 1996 and 1999 followed by a decrease in 1998–1999. Not only did our DInSAR analysis allowed reconstruction of the temporal evolution of vertical land movement, it also provided a detailed account of the shape of uplift and subsidence areas, as a function of mapping of interferometric fringes.

The DInSAR analysis certainly provides an efficient tool to monitor the short-term variations, which are partly related to the status of the water tables influenced by both the seasonal effect and the human over-pumping. To this respect, despite large uncertainties, we could evaluate the ratio between the pumping effect near the Earth's surface and the deep-seated subsidence, for the coastal area of the south-eastern Pingtung Plain where subsidence is largest (as indicated by average subsidence rates of about $+17$ mm/year for the 1995–2005 period, when compared with an average subsidence rate of -6 mm/year for the Holocene). The most important uncertainty in such evaluations certainly depends on the assumption of a constant rate of deep-seated subsidence, which is subject to debate. However, in the case of the Pingtung Plain, the geodetic (GPS) data about horizontal displacements did not reveal large variations during the observation period (1995–2005). It is consequently reasonable to consider that the deep-seated source of deformation did not undergo large variations during this period, which suggests that most of the changes in vertical motion result from underground water status, regardless of its natural or human origin. Like the horizontal displacements, the remaining vertical land movement depends on the tectonic factor and reflects the deformation of the upper lithosphere, which is characterised by significant extension related to extrusion towards the south-west (Angelier et al. 2009; Hu et al. 2006, 2007). This extrusion results from lateral escape in the transition zone between collision and subduction near the southern tip of the Taiwan mountain belt.

Acknowledgments The GPS and levelling data were provided by the Central Geological Survey and the Water Resources Agency of the Ministry of Economic Affairs.

References

Angelier J, Chang TY, Hu JC, Chang CP, Siame L, Lee JC, Deffontaines B, Chu HT, Lu CY (2009) Does extrusion occur at both tips of the Taiwan collision belt? Insights from active deformation studies in the Ilan Plain and Pingtung Plain regions. Tectonophysics 466(3–4):356–376

Berardino P, Fornaro G, Lanari R, Sansosti E (2002) A new algorithm for surface deformation monitoring based on small baseline differential SAR interferograms. IEEE Trans Geosci Remote Sens 40(11):2375–2383

Bürgmann RP, Rosen A, Fielding EJ (2000) Synthetic aperture radar interferometry to measure Earth surface topography and its deformation. Ann Rev Earth Planet Sci 28:169–209

Chang CP, Chang TY, Wang CT, Kuo CH, Chen KS (2004a) Land-surface deformation corresponding to seasonal ground-water fluctuation, determining by SAR interferometry in SW Taiwan. Math Comput Simul 67(4–5):351–359

Chang CP, Wang CT, Chang TY, Chen KS, Liang LS, Pathier E, Angelier J (2004b) Application of SAR interferometry to a large thrust deformation: the 1999 Mw = 7.6 Chichi earthquake in central Taiwan. Geophys J Int 159(1):9–16

Chang CP, Yen JY, Hooper A, Chou FM, Chen YA, Hou CS, Hung WC, Lin MS (2010) Monitoring of surface deformation in northern Taiwan using DInSAR and PSInSAR techniques. Terr Atom Ocean Sci 21(3):447–461

Chen CW, Zebker HA (2000) Network approaches to two-dimensional phase unwrapping: intractability and two new algorithm. J Opt Soc Am A 17:401–414
Chiang CS, Yu HS, Chou YW (2004) Characteristics of the wedge-top depozone of the southern Taiwan foreland basin system. Basin Res 16(1):65–78
Colesanti C, Ferretti A, Prati C, Rocca F (2003) Monitoring landslides and tectonic motions with the permanent scatterers technique. Eng Geol 68(1–2):3–14
Crosetto M, Castillo M, Arbiol M (2003) Urban subsidence monitoring using radar interferometry: algorithms and validation. Photogram Eng Remote Sens 69(7):775–783
Ding XL, Liu GX, Li ZW, Li ZL, Chen YQ (2004) Ground subsidence monitoring in Hong Kong with satellite SAR interferometry. Photogramm Eng Remote Sens 70(10):1151–1156
Ferretti A, Prati C, Rocca F (2000) Nonlinear subsidence rate estimation using permanent scatterers in differential SAR interferometry. IEEE Trans Geosci Remote Sens 38(5):2202–2212
Ferretti A, Prati C, Rocca F (2001) Permanent scatterers in SAR interferometry. IEEE Trans Geosci Remote Sens 39(1):8–20
Fruneau B, Pathier E, Raymond D, Deffontaines B, Lee CT, Wang HT, Angelier J, Rudant JP, Chang CP (2001) Uplift of Tainan Tableland (SW Taiwan) revealed by SAR interferometry. Geophys Res Lett 28(16):3071–3074
Gabriel AK, Goldstein RM, Zebker HA (1989) Mapping small elevation changes over large areas: differential radar interferometry. J Geophys Res 94(B7):9183–9191
Gens R, Genderen JLV (1996) SAR Interferometry: issues, techniques, applications. Intl J Remote Sens 17(10):1803–1836
Ho CS (1986) A synthesis of the geological evolution of Taiwan. Tectonophysics 125(1–3):1–16
Hooper A, Zebker H, Segall P, Kampes B (2004) A new method for measuring deformation on volcanoes and other natural terrains using InSAR persistent scatterers. Geophys Res Lett 31(23):L23611, 1–5
Hou CS, Hu JC, Shen LC, Wang JS, Chen CL, Lai TC, Huang C, Yang YR, Chen RF, Chen YG, Angelier J (2005) Estimation of subsidence using GPS measurements, and related hazard: the Pingtung Plain, southwestern Taiwan. Comptes Rendus Geosci 337(13):1184–1193
Hsieh CS, Shih TY (2006) Coseismic deformation of Chi–Chi earthquake as detected by differential synthetic aperture radar interferometry and GPS data. Terr Atmos Ocean Sci 17(3):517–532
Hsieh ML, Lai TH, Wu LC, Lu WC, Liu HT, Liew PM (2006) Eustatic sea-level change of 11–5 ka in western Taiwan, constrained by radiocarbon dates of core sediments. Terr Atmos Ocean Sci 17(2):353–370
Hu JC, Angelier J, Yu SB (1997) An interpretation of the active deformation of southern Taiwan based on numerical simulation and GPS studies. Tectonophysics 274(1–3):145–169
Hu JC, Yu SB, Angelier J, Chu HT (2001) Active deformation of Taiwan from GPS measurements and numerical simulations. J Geophys Res 106:2265–2280
Hu JC, Chu HT, Hou CS, Lai TH, Chen RF, Nien PF (2006) The contribution to tectonic subsidence by groundwater abstraction in the Pingtung area, southwestern Taiwan as determined by GPS measurements. Quarter Int 147(1):62–69
Hu JC, Hou CS, Shen LC, Chan YC, Chen RF, Huang C, Rau RJ, Chen HH, Lin CW, Huang MH, Nien PF (2007) Fault activity and lateral extrusion inferred from velocity Weld revealed by GPS measurements in the Pingtung area of southwestern Taiwan. J Asian Earth Sci 31(3):287–302
Huang MH, Hu JC, Hsieh CS, Ching KE, Rau RJ, Pathier E, Fruneau B, Deffontaines B (2006) A growing structure near the deformation front in SW Taiwan as deduced from SAR interferometry and geodetic observation. Geophys Res Lett 33:L12305. doi:10.1029/2005GL025613
Huang MH, Hu JC, Ching KE, Rau RJ, Hsieh CS, Pathier E, Fruneau B, Deffontaines B (2009) Active deformation of Tainan Tableland of southwestern Taiwan based on geodetic measurements and SAR interferometry. Tectonophysics 466(3–4):322–344. doi:10.1016/j.tecto.2007.11.020
Industrial Technology Research Institute (1998) Land subsidence motoring with differential levelling—the coastal area of Pingtong county. Tech. Rep., Water Resources Agency, Ministry of Economic Affairs, Taipei, Taiwan, p 46
Kampes BM (2005) Radar interferometry: persistent scatterer technique. Springer, Germany
Klees R, Massonnet D (1998) Deformation measurements using SAR interferometry: potential and limitations. Geologie En Mijnbouw Neth J Geosci 77(2):161–176
Kuo CH, Chan YC, Wang CH (2001) Subsidence: over withdrawal groundwater, tectonic or both? EOS, Trans AGU 82(47) Fall Meet. Suppl. Abstract H42D-0401
Lai CH, Hsieh ML, Liew PM, Chen YG (2002) Holocene rock uplift and subsidence in the coastal area of Taiwan. EOS, Trans AGU 83(47) Fall Meet. Suppl. Abstract T61B-1273
Lin AT, Watts AB, Hesselbo SP (2003) Cenozoic stratigraphy and subsidence history of the South China Sea margin in the Taiwan region. Basin Res 15(4):453–478

Lin KC, Hu JC, Ching KE, Angelier J, Rau RJ, Yu SB, Tsai CH, Shin TC, Huang MH (2010) GPS crustal deformation, strain rate and seismic activity after the 1999 Chi–Chi earthquake in Taiwan. J Geophys Res 115:B07404

Massonnet D, Feigl KL (1998) Radar interferometry and its application to changes in the earth surface. Rev Geophys 36(4):441–500

Massonnet D, Feigl K, Rossi M, Adragna F (1994) Radar interferometric mapping of deformation in the year after the Landers earthquake. Nature 369:227–230

Pathier E, Fruneau B, Deffontaines B, Angelier J, Chang CP, Yu SB, Lee CT (2003) Coseismic displacements of the footwall of the Chelungpu fault caused by the 1999, Taiwan Chi–Chi earthquake from InSAR and GPS data. Earth Planet Sci Lett 1–2(16):73–88

Peyret M, Rolandone F, Dominguez S, Djamour Y, Meyer B (2008) Source model for the Mw 6.1, 31 March 2006, Chalan–Chulan earthquake (Iran) from InSAR. Terra Nova 20(2):126–133

Rosen PA, Hensley S, Joughin IR, Li FK, Madsen SN, Rodriguez E, Goldstein RM (2000) Synthetic aperture radar interferometry. Proc IEEE 88(3):333–382

Shen LC, Hou CS, Hu JC, Chan YC, Huang C, Lai TC, Lin CW (2003) GPS measurements of active structure in Pingtung area, southwestern Taiwan. Spec Publ Cent Geol Surv 14:165–176

Shyu JBH, Sieh K, Chen YG, Liu CS (2005) Neotectonic architecture of Taiwan and its implications for future large earthquakes. J Geophys Res 110:B08402. doi:10.1029/2004JB003251

Stevens NF, Wadge G (2004) Towards operational repeat-pass SAR interferometry at active volcanoes. Nat. Hazards 33:47–76

Suppe J (1984) Kinematics of arc-continent collision, flipping of subduction and back-arc spreading near Taiwan. Memoir Geol Soc China 6:21–33

Tung H, Hu JC (2011) Assessments of series anthropogenic land subsidence in Yunlin County of central Taiwan from 1996 to 1999 by Persistent Scatterers InSAR. (Submitted to Tectonophysics)

Yu SB, Chen HY, Kuo LC (1997) Velocity field of GPS stations in the Taiwan area. Tectonophysics 274(1–3):41–59

Zebker HA (2000) Studying the Earth with interferometric radar. Comput Sci Eng 2(3):52–60

Zebker HA, Villasenor J (1992) Decorrelation in interferometric radar echoes. IEEE Trans Geosci Remote Sens 30(5):950–959

Zebker HA, Rosen PA, Goldstien RM, Gabriel A, Werner CL (1994) On the derivation of co-seismic displacement fields using differential radar interferometry: the Landers earthquake. J Geophys Res 99(B10):19617–19634